ACS APPLIED MATERIALS & INTERFACES

Research Article

www.acsami.org

Microanalysis of a Grain Boundary's Blocking Effect in Lanthanum Silicate Electrolyte for Intermediate-Temperature Solid Oxide Fuel Cells

Pengfei Yan,*[,†] Atsushi Mineshige,[‡] Toshiyuki Mori,[†] Yuanyuan Wu,[†] Graeme John Auchterlonie,[§] Jin Zou,[§,¶] and John Drennan[§]

[†]Global Research Center for Environmental and Energy based on Nanomaterials Science (GREEN), National Institute for Materials Science, 1-1 Namiki, Tsukuba, Ibaraki 305-0044, Japan

[‡]Department of Materials Science and Chemistry, Graduate school of Engineering, University of Hyogo, 2167 Shosha, Himeji, Hyogo 671-2201, Japan

[§]Centre for Microscopy and Microanalysis and [¶]Materials Engineering, The University of Queensland, Brisbane, QLD 4072, Australia

ABSTRACT: In order to study the grain boundary's (GB's) blocking effect in lanthanum silicate electrolyte, high density Al-doped apatite-type lanthanum silicate was synthesized and characterized by impedance spectroscopy, scanning electron microscopy, X-ray diffraction, and transmission electron microscopy. Microstructural characterization indicated that the GB's blocking effect was an intrinsic effect. Further microanalysis shows that the GB region is rich in La and poor in Si in comparing with the grain interior (GI). Our discussion suggested that the chemical variation from GI to GB, on the one hand, could degrade the GB region's conductivity; on the other hand, it introduced a strong space-charge effect at GBs. The latter was believed to play a dominant role in the GB's blocking effect.

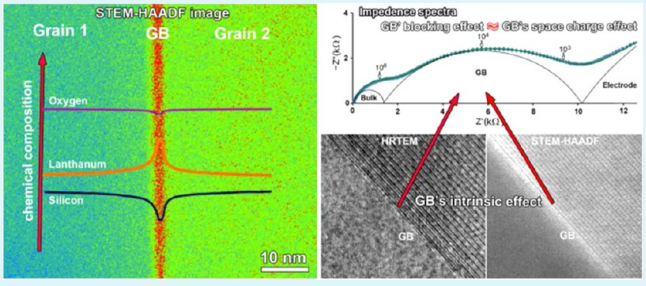

KEYWORDS: *grain boundary, impedance spectroscopy, TEM, lanthanum silicate, space-charge effect*

1. INTRODUCTION

A solid oxide fuel cell (SOFC) can directly transform chemical energy into electrical energy; therefore, its high efficiency (>50%) is a big advantage over the electricity-generator devices that are based on the combustion of fossil fuels.[1,2] A single SOFC device is made up by three components: an anode, cathode, and electrolyte. Materials used as electrolytes should have a good ionic conductivity and negligible electronic conductivity. Yttria-stabilized zirconia (YSZ) is the most commonly used SOFC electrolyte at high temperatures (>800 °C).[3] However, the high operation temperature incurs significant difficulties in material selections for both electrode and interconnected components. When the operation temperature is below 800 °C, YSZ's ionic conductivity becomes too low to achieve high power density in SOFC applications. As a result, many alternative oxide-ion conductors have been explored for intermediate temperature (500−700 °C) SOFC in the past decades, such as doped ceria, $LaGaO_3$-based perovskite, and apatite-type lanthanum silicates.[3−5] The conduction mechanism of apatite-type lanthanum silicates is an interstitial mechanism,[6,7] which is different from the oxygen vacancy diffusion mechanism in doped ceria, $LaGaO_3$-based perovskites, and other electrolytes.[8,9] Theoretical studies suggested that the activation energy of interstitial oxide conduction mechanism was lower than that of oxygen vacancy conduction mechanism.[10,11] Thus, the unique conduction mechanism of lanthanum silicates is an advantage over other electrolytes. Moreover, lanthanum silicate has been found to be tolerant to a broad range of dopants,[12] which provides more opportunities in material design and optimization to achieve high ionic conductivity. Therefore, apatite-type lanthanum silicates are promising electrolytes for intermediate temperature SOFCs.

Hexagonal apatite-type lanthanum silicate is a cation-deficient structure with its chemical formula as $La_{9.33+x}Si_6O_{26+1.5x}$ (LSO), in which La-site vacancies are formed. The ionic conductivity of hexagonal apatite-type lanthanum silicate was first evaluated by Nakayama et al in 1995.[13] It was reported that the material had a very low activation energy (0.7 eV) and good conductivity (1.4×10^{-3} S/cm at 700 °C). Since then many researchers were engaged in developing higher conductive lanthanum silicates as well as the conduction mechanism in lanthanum silicates.[6,11,14−22] Recently, Fukuda et al. reported that the *c*-axis-conductivity of lanthanum silicate could be as high as 7.9×10^{-2} S/cm at 800 °C and the activation energy was as low as 0.35 eV.[23]

Received: April 2, 2013
Accepted: May 22, 2013
Published: May 22, 2013

In the past decades, studies on LSO-based materials mainly related to their bulk conductivity. Less attention was paid to the grain boundary's (GB's) conductivity, even though impedance spectroscopy has repeatedly shown that a GB's blocking effect is significant.[19,24−26] Since LSO-based materials are presented as a polycrystalline form in SOFC application, to improve the total conductivity, it is very necessary to minimize GB's blocking effect in LSO-based electrolytes. According to previous reports on zirconia-based and ceria-based electrolytes, the GB's blocking effect was categorized into extrinsic effect and intrinsic effect.[27−29] The former is due to the formation of an intergranular impurity phase. The latter comes from GB itself. It is still unclear which effect dominates the GB's blocking effect in LSO-based electrolytes. More detailed studies on GB's structure−property relationship are needed for lanthanum silicates in order to understand the GB's blocking effect and improve the total conductivity. In this work, a highly dense Al-doped apatite-type LSO pellet was synthesized. Its high GB blocking effect was studied by diverse analytical techniques including impedance spectroscopy, scanning electron microscope (SEM), X-ray diffraction (XRD), and transmission electron microscopy (TEM). The structure−property relation was analyzed, which could benefit our understanding of the high GB blocking effect in such typical apatite-type lanthanum silicate and provide useful information for developing highly conductive LSO-based electrolytes.

2. EXPERIMENTAL SECTION

Due to the strong enhancement of conductivity in lanthanum silicates by Al-doping effect,[20] the hexagonal Al-doped LSO electrolytes are very promising. In this work, Al-doped LSO (ALSO, with nominal chemical formula as $La_{9.33+x}Si_{5.8}Al_{0.2}O_{25.9+1.5x}$) was synthesized by conventional solid-state reaction. Specimens were obtained from a mixture of raw powders of La_2O_3 (99.99% purity, Kishida Chemical Co. Ltd.), SiO_2 (99% purity, Kishida Chemical Co. Ltd.), and $Al(OH)_3$ (99.5% purity, Kishida Chemical Co. Ltd.). Powders were pressed into a disc at 57 MPa, followed by sintering at 1700 °C for 10 h in air. To make the pellets fully dense, the calcined powders were thoroughly ground in ethanol for 2 h with a planetary ball mill at a rotating speed of 400 rpm before the final sintering.

The sintered ALSO pellet was mechanically polished to a thickness of 1.3 mm by removing both sides of the surface. After that, circular Pt paste areas were applied to both surfaces with their diameters as 6 mm. Then, they were fired at 1000 °C for 2 h to serve as electrodes. The impedance spectra were obtained by Solartron SI 1260 impedance spectroscopy with ac amplitude as 80 mV and a frequency range of 10^6−0.1 Hz. The ALSO sample was measured from 250 to 375 °C with an interval of 25 °C. The impedance spectra were fitted according to an equivalent circuit with the program ZView (Version 3.0a). The Q is a constant phase element, which is characterized by two parameters, C_Q and n. Corresponding capacitances, C, were obtained from $C = (R^{1-n}C_Q)^{1/n}$.

After impedance spectroscopy measurements, the Pt electrodes were removed and the specimen was characterized by X-ray diffraction (XRD) (RINT-ULTMA+) with Cu Kα_1 as the X-ray source. The collecting 2θ angle was from 10° to 90°. Then, after a thermal etching of the sample at 1500 °C for 1 h, scanning electron microscope (SEM) (JEOL S-5000) was applied to observe the microstructure. After that TEM specimens were prepared by conventional grinding and dimpling, and finished by Ar ion-milling using Gatan PIPS model 691 ion-milling machine. To minimize the damage from the ion-milling process, a low ion-beam voltage of 3.5 keV and a small incident beam angle (5°) were used for final thinning. TEM investigations were performed on a JEOL 2100F TEM operated at 200 kV. The TEM is equipped with energy dispersive X-ray spectroscopy (EDS) and high-angle annular dark-field (HAADF) detector for chemical analysis. The electron beam probe size was set to 0.2 nm for STEM-HAADF imaging and 1 nm for EDS measurement in the scanning-TEM (STEM) model. The inner and outer angles of the HAADF detector were 190 and 470 mrad, respectively. Inelastic scattering was expected to be dominant under this condition for lanthanum silicate.

3. RESULTS

3.1. Impedance Spectroscopy. Since the secondary phase in our ALSO sample is negligible (see the following Microstructure Characterization section), it is reasonable to treat our ALSO sample as a homogeneous material. Thus, the electrical response of our ALSO sample can be described using the brick-layer model.[30] Impedance spectra of the ALSO sample always show three semicircle arcs in all measured temperature points. Figure 1 shows a representative impedance

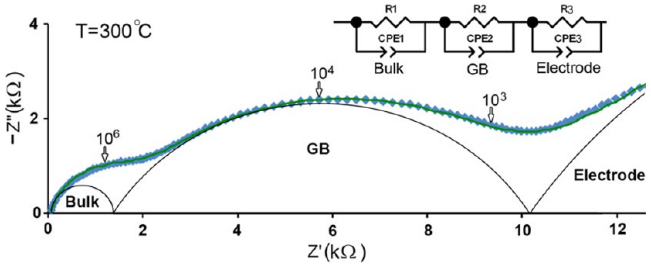

Figure 1. Impedance spectrum of the ASLO sample measured at 300 °C. The fitting curve is plotted according to the equivalent circuits (shown in the top right corner). The deconvolution of contributions from bulk, GB, and electrode are also plotted.

spectrum of the ALSO at 300 °C. According to the brick-layer model, the two semicircles in higher frequency range were assigned to the impedance response of the grain interior (GI) and GB, respectively. The third one was assigned to electrode polarization. By fitting the experimental impedance spectra with an equivalent circuit (shown in Figure 1), the resistances and capacitances both from bulk and GB can be obtained (shown in Table 1). Our impedance results are consistent with previous

Table 1. Fitting Results at Different Temperature (T): Bulk Resistance R_{GI}, Bulk Capacitance C_{GI}, GB Resistance R_{GB}, and GB Capacitance C_{GB}

T (°C)	R_{GI} (Ω)	C_{GI} (10^{-11}F)	R_{GB} (Ω)	C_{GB} (10^{-9} F)
250	4529	8.68	40032	5.06
275	2460	8.76	18100	5.83
300	1512	8.58	8578	5.17
325	811	9.89	4696	5.55
350	519	10.27	2606	5.13
375	366	9.34	1368	5.37

impedance analysis of LSO samples.[19,24−26] As can be seen in Figure 1 and Table 1, the GB's resistances are much larger than corresponding bulk resistances in our measured temperature range (250−375 °C). Therefore, the GB's blocking effect in our ALSO sample is very significant and its influence on the overall ionic conductivity is of great concern.

In order to estimate the GB's conductivity, we assumed the dielectric constants of GI and GB are the same, according to eq 1,[29]

$$\delta = \left(\frac{C_{GI}}{C_{GB}}\right)\cdot D \qquad (1)$$

where C_{GI} and C_{GB} are the capacitance values of GI and GB, respectively; D is the average grain size. The estimated GB thickness, δ, is around 90 nm for our ALSO sample, which is close to the previously reported value (70 nm).[24] According to GI and GB's resistances at different temperatures (Table 1), temperature dependent conductivities both from GI (i.e., bulk) and GB were obtained and plotted in Figure 2. According to

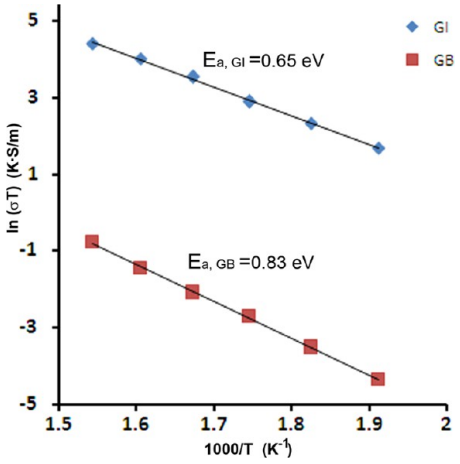

Figure 2. Temperature dependent conductivity of GI and GB. According to the Arrhenius equation, the activation energy values are 0.65 and 0.83 eV for GI and GB, respectively.

the Arrhenius equation, $\sigma T = A \exp(-\Delta E/RT)$, where σ is the conductivity, T is the absolute temperature, and R is the gas constant. The activation energy of GI ($E_{a,GI}$) and GB ($E_{a,GB}$) were estimated as 0.65 and 0.83 eV (shown in Figure 2), respectively. Their values are consistent with previous reports.[13,20] GB activation energy is higher than that of GI, which also indicates GB acts as a blocking layer for the conduction of oxide ions.

3.2. Microstructure Characterization. *3.2.1. SEM and XRD.* SEM observation shows that only a few small pores were formed within the sintered ALSO sample (shown in Figure 3), which indicates that the ASLO pellet is highly dense (~97%). Our ALSO samples are in the form of polycrystalline. Most of grains are in the range of 3−10 μm in size. The average grain size (D) is estimated as 5 μm according to SEM images. XRD

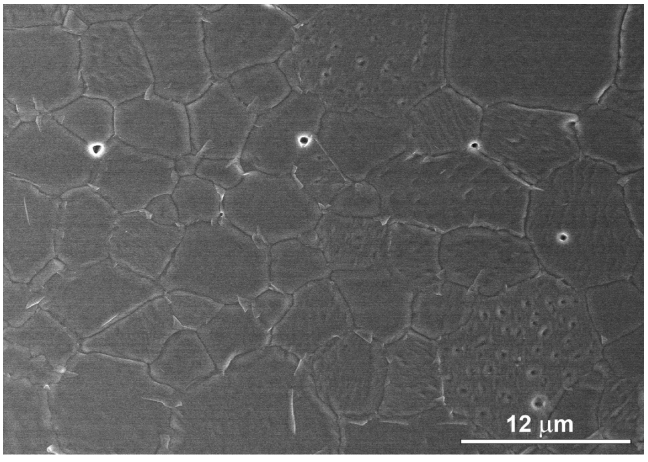

Figure 3. SEM micrograph to show the dense morphology of the sintered ALSO sample.

was also employed to examine the ASLO sample. As shown in Figure 4, all the peaks in the XRD pattern were attributed to

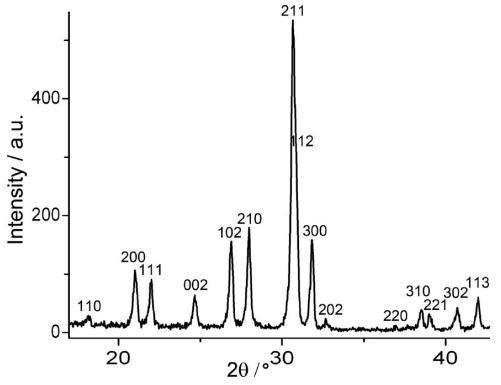

Figure 4. XRD pattern indicates that the prepared ALSO sample shows high phase purity. All the peaks are indexed by the hexagonal apatite-type structure.

the hexagonal apatite-type structure, which indicated that an impurity phase, if it existed, was successfully depressed to a very low level.

3.2.2. TEM Characterization. In grain interiors, hexagonal apatite-type structure was confirmed by TEM through both selected area electron diffraction (SAED) patterns and high resolution lattice images. Representative TEM results were shown in Figure 5a, b, and d. Figure 5c shows the crystal structure of hexagonal apatite-type lanthanum silicate viewed along the [111] zone axis. By comparing d with c, it was noted that only La-site atomic columns were visible in STEM-HAADF lattice image (Figure 5d). Thus, the brightness of the STEM-HAADF image mainly comes from La's inelastic scattering of electrons.

In GB areas, our intensive TEM observation confirmed that most GBs were free of impurity phase. However, small-size impurity phases were found at grains' triple junction positions (as shown in Figure 6a). EDS results showed that the impurity phase was rich in La and poor in Si and impurity element P was also detected within it (shown in Figure 6b and c). The formation of impurity phase is probably due to the low purity of precursors (99% SiO_2 and 99.5% $Al(OH)_3$). However, impurity phases only formed at grains' triple junction positions. Since such an impurity phase is very small and its distribution is very few, it can hardly cause significant conductivity degradation in our samples. Thus, the high GB's blocking effect in our sample is not due to a GB's intergranular impurity phases. Further HRTEM images and high resolution STEM-HAADF lattice images also confirmed that grains were directly connected. Representative lattice images of a GB are shown in Figure 7. It shows a direct grain-to-grain connected GB. According to our atomic TEM observation, it was confirmed that the GB's blocking effect is an intrinsic effect. Our experiment also evidenced that even using low purity precursors to synthesize LSO-based electrolyte the extrinsic effect was still neglectable in blocking oxide ions.

However, we noted that GBs had a bright contrast under STEM-HAADF mode (shown in Figure 7b and Figure 8). Since the brightness of HAADF image is mainly contributed by La-site atomic columns (See Figure 5d, a high atomic number resulting in high electron scattering ability[31]), the GB's bright contrast indicated a local enrichment of La at GBs. Further

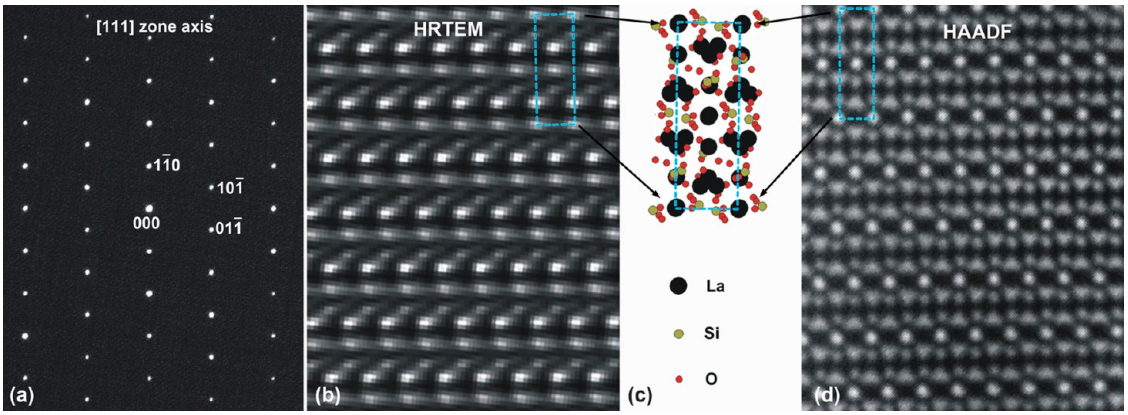

Figure 5. TEM results from the sample's [111] zone axis: (a) SAED pattern; (b) HRTEM image; (d) STEM-HAADF image. (c) Lattice structure of hexagonal apatite-type $La_{9.33}Si_6O_{26}$ projected from the [111] zone axis. Comparing c with d, it was found that bright spots in STEM-HAADF image were corresponding to La-site atomic columns.

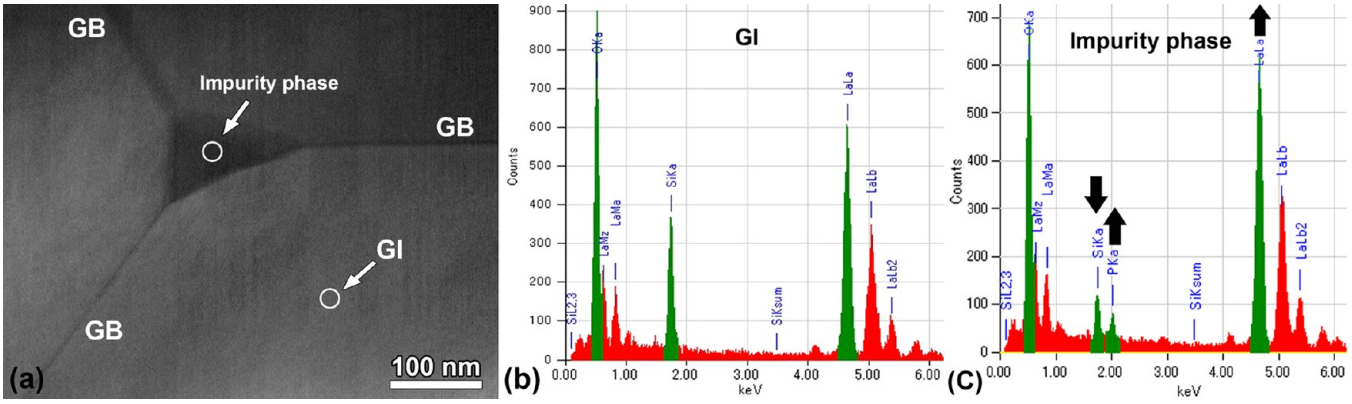

Figure 6. (a) STEM bright field image showing GBs and impurity phase at grain's triple junction. (b) EDS spectrum from grain interior as indicated by "GI" in part a. (c) EDS spectrum from impurity phase as indicated by "Impurity phase" in part a. Comparing b with c, it can be seen that the impurity phase is rich in La and poor in Si and contains impurity element P.

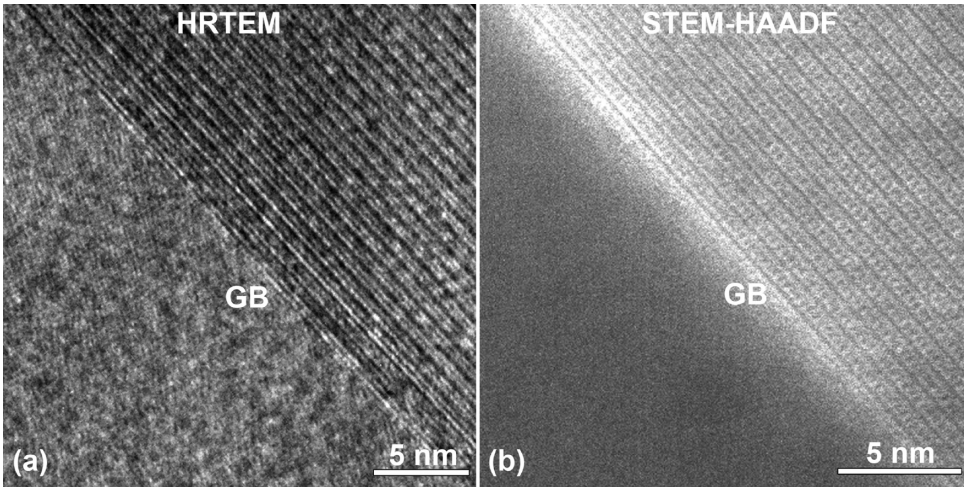

Figure 7. Typical GB region imaging with (a) HRTEM and (b) high resolution STEM-HAADF. Both images show that the GB is sharp and clean.

EDS measurement confirmed such chemical variation between GI and GB. Figure 9 shows quantitative EDS line-scan results of GB and GI. Compared with GI, GB is rich in La and poor in Si. On the basis of each element's concentration (average values in Figure 9b) and the charge neutrality principle, the chemical formulas for GI and GB are approximately $La_{9.33}Si_6O_{26}$ and $La_{10}Si_5O_{25}$, respectively. (The small amount of Al-dopant (less than 1%) is neglectable.) Our TEM results also indicated that such an abnormal GB apatite layer was very thin (a few nanometers). It is necessary to point out that because of the interfacial features the local composition of GB is usually different with GI,[32] especially for ionic solids.[33] The estimated chemical formulas indicated that GI was a common La-deficient LSO but GB was an oxygen-and-silicon-deficient LSO.

dx.doi.org/10.1021/am401195e | ACS Appl. Mater. Interfaces 2013, 5, 5307−5313

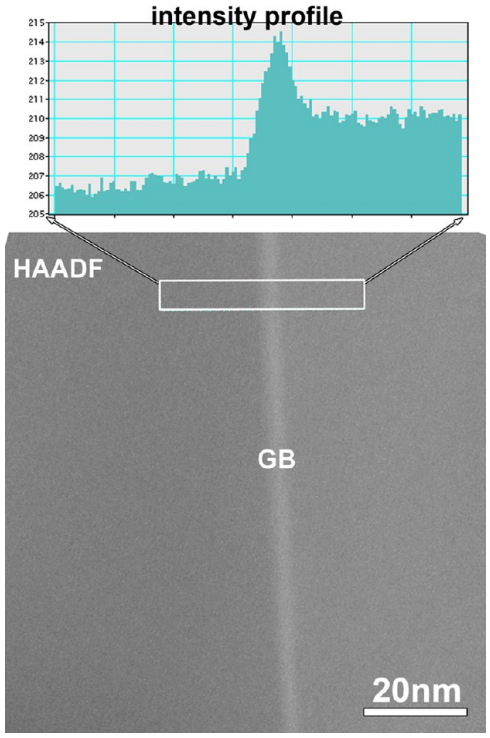

Figure 8. GB's bright contrast is clear in the low magnification STEM-HAADF image. The intensity profile across the GB is also given.

4. DISCUSSION

4.1. Structural and Chemical Analysis. Due to the interstitial conduction mechanism of LSO-based electrolytes, material's conductivity is very sensitive to the concentration of interstitial oxide ions. Therefore, oxygen excess LSO materials ($La_{9.33+x}Si_6O_{26+1.5x}$, $0 < x < 0.67$) show very high ionic conductivity.[6,11,16,20,22] In this work, our EDS analysis indicates GB's chemical formula is $La_{10}Si_5O_{25}$. Though there is no data about the conductivity of such composition LSO material, it is reasonable to believe its conductivity is very low. First, GB's chemical composition ($La_{10}Si_5O_{25}$) indicates that GB is an oxygen-deficient LSO layer. There are many oxygen vacancies within the GB region. Interstitial oxide ions prefer to fall into oxygen-sites. Therefore, interstitial oxide ions can hardly exist in such oxygen-deficient LSO structure, which will results in the GB region as a depletion layer of interstitial oxide ions. According to the interstitial conduction mechanism of apatite-type LSO, the GB region will exhibit very low conductivity. Second, the GB's chemical composition deviates from normal apatite-type lanthanum silicate, which can result in severe lattice distortion and influence the diffusion path of oxide ions. Finally, few la-site vacancies at GBs also play a negative role in oxide ion conduction.[21,22]

Additionally, the GB's chemical composition seems close to the La_2SiO_5 second phase, which probably indicates that the GB's chemical variation favors the formation of La_2SiO_5 second phase at GBs. Because in our previous ALSO samples,[17] a small amount of the La_2SiO_5 second phase was detected by XRD.

4.2. Space-Charge Analysis. In the view of crystallography, the GB is the place where bulk lattice symmetry is broken. Therefore, the GB structure is a nonequilibrium state compared with the GI. Consequently, structural and chemical variation between GB and GI always happens, which can result in the formation of charged regions near GBs in ionic solids.[34,35] It has been verified that such charged GB regions played a significant role in determining the conductivity of many electrolytes.[28,29,36−38] Because GB may act as barrier layer when free carriers try to diffuse across a GB, which is the well-known space-charge effect.[28] In this work, our TEM characterization already confirmed local chemical variation at GBs. However, it is still unclear whether this chemical variation will result in a strong space-charge effect. It is also unclear whether the space-charge effect plays a dominant role in GB's blocking effect. To address these issues, we conducted a space-charge analysis as follows.

If a GB's blocking effect is mainly due to its space-charge effect, according to the Schottky barrier model,[28]

$$\frac{\sigma_{GI}}{\sigma_{GB}} = \frac{\exp(ze\Delta\varphi(0)/k_BT)}{2ze\Delta\varphi(0)/k_BT} \quad (2)$$

where σ_{GI} is the grain-interior's (bulk) conductivity; σ_{GB} is the GB's conductivity; $\Delta\varphi(0)$ is the Schottky barrier height or the space-charge potential;[28] e is the elementary charge; z is the charge number; k_B is Boltzmann's constant, and T is the absolute temperature. The Schottky barrier height, $\Delta\varphi(0)$, can

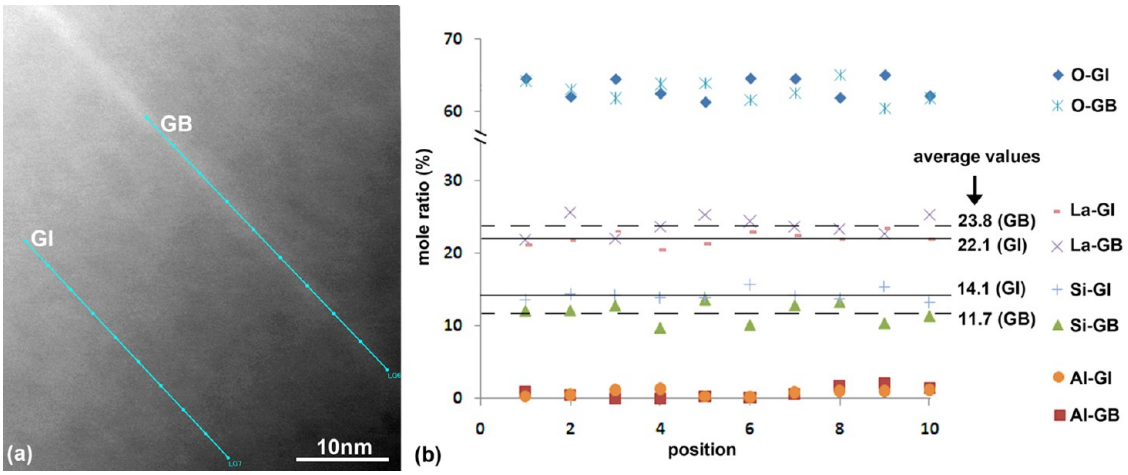

Figure 9. EDS line scans both from GI and GB. The locations were shown in part a. Quantitative composition results were shown in b. The average values indicated that the GB region is rich in La and poor in Si.

dx.doi.org/10.1021/am401195e | ACS Appl. Mater. Interfaces 2013, 5, 5307−5313

be estimated from eq 2. Figure 10 shows temperature dependent $\Delta\varphi(0)$ for our ALSO sample.

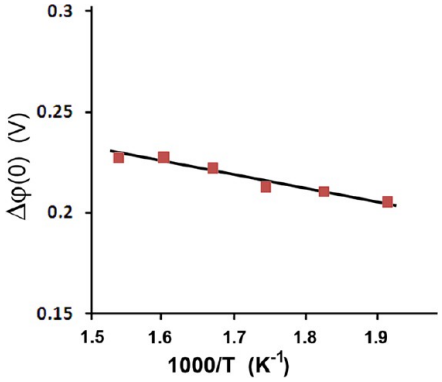

Figure 10. Temperature dependent Schottky barrier heights ($\Delta\varphi(0)$).

Due to the Schottky barrier layer, a higher activation energy of GB ($E_{a,GB}$) is required compared with GI ($E_{a,GI}$). According to the space-charge theory, their energy difference ΔE_c can be calculated by using eq 3:[28]

$$\Delta E_c = (2e\Delta\varphi(0) - k_B T)\left\{1 + \frac{1}{T\Delta\varphi(0)}\frac{\partial\Delta\varphi(0)}{\partial(1/T)}\right\} \quad (3)$$

As demonstrated by Guo et al.,[28,29] if GB's blocking effect is due to GB's space-charge effect, the average value of ΔE_c calculated from eq 3 should agree well with the experimental result (ΔE_m), i.e. $\overline{\Delta E}_c \approx \Delta E_m$. For our ALSO sample, $\overline{\Delta E}_c$ is estimated as 0.2 eV, which is in good agreement with ΔE_m (0.18 eV) ($\Delta E_m = E_{a,GB} - E_{a,GI}$). Therefore, we believe that GB's blocking effect is mainly due to GB's space-charge effect.

On the basis of our above analysis, it is believed that the chemical composition variation from GI to GB resulted in a strong space-charge effect at GBs. It is very essential to minimize GB's blocking effect to obtain highly conductive LSO electrolytes. During the past decades, substantial studies have been done on the space-charge theory, which provided theoretical instructions on how to minimize GB's space-charge effect in solid state electrolytes. Simultaneously, many novel material-processing methods have been explored in many kinds of electrolytes to reduce the GB's space-charge effect.[39−43] Such theoretical and experimental works, as well as our microanalysis in this work, can provide valuable indications for minimizing the GB's blocking effect in lanthanum silicates.

5. CONCLUSION

Structural characterization confirmed that a GB's blocking effect was an intrinsic effect in our ALSO electrolyte. Further microanalysis on GB regions found that the chemical composition at the GB was different than that in the GI, i.e. the GB was rich in La and poor in Si. Our analysis indicated that such local chemical variation at the GB region results in not only a low conductivity GB layer but also a strong space-charge effect at GB. A GB's space-charge effect was believed to play a dominant role in a GB's blocking effect, which is valuable for design and synthesis of high performance LSO-based electrolytes. Our work contributed to the understanding of GB's structure−property relation in LSO-based electrolytes.

AUTHOR INFORMATION

Corresponding Author

*E-mail address: YAN.Pengfei@nims.go.jp.

Notes

The authors declare no competing financial interest.

ACKNOWLEDGMENTS

Financial support from the Grant-in-Aid for Scientific Research (22310053) by the Ministry of Education, Culture, Sports, and Technology (MEXT), Japan, is gratefully acknowledged. The authors also appreciate the partial funding support from Global Research Center for Environment and Energy based on Nanomaterials Science (GREEN), National Institute for Materials Science, Japan. P.Y. thanks Mr. A. Suzuki for his assistance in ac impedance measurement.

REFERENCES

(1) Steele, B. C. H.; Heinzel, A. *Nature* **2001**, *414*, 345−352.
(2) Ormerod, R. M. *Chem. Soc. Rev.* **2003**, *32*, 17−28.
(3) Fergus, J. W. *J. Power Sources* **2006**, *162*, 30−40.
(4) Huijsmans, J. P. P.; van Berkel, F. P. F.; Christie, G. M. *J. Power Sources* **1998**, *71*, 107−110.
(5) Inaba, H.; Tagawa, H. *Solid State Ionics* **1996**, *83*, 1−16.
(6) León-Reina, L.; Losilla, E. R.; Martínez-Lara, M.; Bruque, S.; Llobet, A.; Sheptyakov, D. V.; Aranda, M. A. G. *J. Mater. Chem.* **2005**, *15*, 2489−2498.
(7) Matsunaga, K.; Toyoura, K. *J. Mater. Chem.* **2012**, *22*, 7265−7273.
(8) Gangopadhayay, S.; Inerbaev, T.; Masunov, A. m. E.; Altilio, D.; Orlovskaya, N. *ACS Appl. Mater. Interfaces* **2009**, *1*, 1512−1519.
(9) Ganopadhyay, S.; Masunov, A. E.; Inerbaev, T.; Mesit, J.; Guha, R. K.; Sleiti, A. K.; Kapat, J. S. *Solid State Ionics* **2010**, *181*, 1067−1073.
(10) Tolchard, J. R.; Islam, M. S.; Slater, P. R. *J. Mater. Chem.* **2003**, *13*, 1956−1961.
(11) Béchade, E.; Masson, O.; Iwata, T.; Julien, I.; Fukuda, K.; Thomas, P.; Champion, E. *Chem. Mater.* **2009**, *21*, 2508−2517.
(12) Tolchard, J. R.; Slater, P. R.; Islam, M. S. *Adv. Funct. Mater.* **2007**, *17*, 2564−2571.
(13) Nakayama, S.; Kageyama, T.; Aono, H.; Sadaoka, Y. *J. Mater. Chem.* **1995**, *5*, 1801−1805.
(14) Kendrick, E.; Islam, M. S.; Slater, P. R. *J. Mater. Chem.* **2007**, *17*, 3104−3111.
(15) Panteix, P. J.; Julien, I.; Bernache-Assollant, D.; Abélard, P. *Mater. Chem. Phys.* **2006**, *95*, 313−320.
(16) Slater, P. R.; Sansom, J. E. H.; Tolchard, J. R. *Chem. Rec.* **2004**, *4*, 373−384.
(17) Mineshige, A.; Ohnishi, Y.; Sakamoto, R.; Daiko, Y.; Kobune, M.; Yazawa, T.; Yoshioka, H.; Nakao, T.; Fukutsuka, T.; Uchimoto, Y. *Solid State Ionics* **2011**, *192*, 195−199.
(18) Tolchard, J. R.; Slater, P. R. *J. Phys. Chem. Solids* **2008**, *69*, 2433−2439.
(19) Chefi, S.; Madani, A.; Boussetta, H.; Roux, C.; Hammou, A. *J. Power Sources* **2008**, *177*, 464−469.
(20) Abram, E. J.; Sinclair, D. C.; West, A. R. *J. Mater. Chem.* **2001**, *11*, 1978−1979.
(21) Sansom, J. E. H.; Richings, D.; Slater, P. R. *Solid State Ionics* **2001**, *139*, 205−210.
(22) Yoshioka, H. *J. Am. Ceram. Soc.* **2007**, *90*, 3099−3105.
(23) Fukuda, K.; Asaka, T.; Oyabu, M.; Urushihara, D.; Berghout, A.; Bechade, E.; Masson, O.; Julien, I.; Thomas, P. *Chem. Mater.* **2012**, *24*, 4623−4631.
(24) Porras-Vázquez, J. M.; Losilla, E. R.; León-Reina, L.; Marrero-López, D.; Aranda, M. A. G. *J. Am. Ceram. Soc.* **2009**, *92*, 1062−1068.
(25) Marrero-López, D.; Martín-Sedeño, M. C.; Peña-Martínez, J.; Ruiz-Morales, J. C.; Núñez, P.; Aranda, M. A. G.; Ramos-Barrado, J. R. *J. Power Sources* **2010**, *195*, 2496−2506.

(26) Chesnaud, A.; Dezanneau, G.; Estournès, C.; Bogicevic, C.; Karolak, F.; Geiger, S.; Geneste, G. *Solid State Ionics* **2008**, *179*, 1929−1939.
(27) Badwal, S. P. S.; Drennan, J. *J. Mater. Sci.* **1987**, *22*, 3231−3239.
(28) Guo, X.; Waser, R. *Prog. Mater. Sci.* **2006**, *51*, 151−210.
(29) Guo, X.; Maier, J. *J. Electrochem. Soc.* **2001**, *148*, E121−E126.
(30) Bonanos, N.; Steele, B. C. H.; Butler, E. P. *Impedance Spectroscopy Theory, Experiment, and Applications*, second ed.; Barsoukov, E., Macdonald, J. R., Eds.; John Wiley & Sons, Inc.: Hoboken, NJ, 2005; Chapter 4, p 129.
(31) Pennycook, S. J.; Boatner, L. A. *Nature* **1988**, *336*, 565−567.
(32) Dillon, S. J.; Tang, M.; Carter, W. C.; Harmer, M. P. *Acta Mater.* **2007**, *55*, 6208−6218.
(33) Lei, Y. Y.; Ito, Y.; Browning, N. D.; Mazanec, T. J. *J. Am. Ceram. Soc.* **2002**, *85*, 2359−2363.
(34) Maier, J. *Solid State Ionics* **2003**, *157*, 327−334.
(35) Maier, J. *Nat. Mater.* **2005**, *4*, 805−815.
(36) Guo, X.; Sigle, W.; Fleig, J.; Maier, J. *Solid State Ionics* **2002**, *154*, 555−561.
(37) Gerhardt, R.; Nowick, A. S. *J. Am. Ceram. Soc.* **1986**, *69*, 641−646.
(38) Avila-Paredes, H. J.; Choi, K.; Chen, C.-T.; Kim, S. *J. Mater. Chem.* **2009**, *19*, 4837−4842.
(39) Mori, T.; Kobayashi, T.; Wang, Y.; Drennan, J.; Nishimura, T.; Li, J. G.; Kobayashi, H. *J. Am. Ceram. Soc.* **2005**, *88*, 1981−1984.
(40) Gregori, G.; Lupetin, P.; Maier, J. *ECS Trans.* **2012**, *45*, 19−24.
(41) Lupetin, P.; Giannici, F.; Gregori, G.; Martorana, A.; Maier, J. *J. Electrochem. Soc.* **2012**, *159*, B417−B425.
(42) Avila-Paredes, H. J.; Kim, S. *Solid State Ionics* **2006**, *177*, 3075−3080.
(43) Litzelman, S. J.; De Souza, R. A.; Butz, B.; Tuller, H. L.; Martin, M.; Gerthsen, D. *J. Electroceram.* **2009**, *22*, 405−415.